

Efficient algorithm for calculating transposed PSF matrices for 3D light field deconvolution

MARTIN EBERHART, High Enthalpy Flow Diagnostics Group, Institute of Space Systems, University of Stuttgart

Volume reconstruction by 3D light field deconvolution is a technique that has been successfully demonstrated for microscopic images recorded by a plenoptic camera. This method requires to compute a transposed version of the 5D matrix that holds the point spread function (PSF) of the optical system. For high resolution cameras with hexagonal microlens arrays this is a very time consuming step. This paper illustrates the significance and the construction of this special matrix and presents an efficient algorithm for its computation, which is based on the distinct relation of the corresponding indices within the original and the transposed matrix. The required computation time is, compared to previously published algorithms, significantly shorter.

Additional Key Words and Phrases: light fields, volume reconstruction, deconvolution

ACM Reference format:

Martin Eberhart. 2016. Efficient algorithm for calculating transposed PSF matrices for 3D light field deconvolution. 1, 1, Article 1 (January 2016), 7 pages.

DOI: 10.1145/nnnnnnn.nnnnnnn

1 INTRODUCTION

Modern digital image sensors are the result of a remarkable evolution that has its roots in the chemical photographic films, dating back to the late 19th century. These films are based on the blackening of silver halide particles by incident light, and roughly a hundred years later, the light sensitive crystals were replaced by silicon pixels in the first electronic cameras [12]. Since then, the sensors featured ever increasing spatial resolution, sensitivity and dynamic range. But as their chemical ancestors, digital image sensors still are flat, planar devices and record two-dimensional projections of the three-dimensional reality. The same is true for the retina, the biological image sensor of our eyes. However, nature has doubled this organ, and the brain can derive the third dimension from the perspectively shifted images seen by two spatially separated eyes. Such stereo vision has also been adopted by digital systems. It operates on sets of two or more images recorded from different viewpoints, either by translating a single camera or using a setup of several devices in parallel. An important requirement is the presence of patterns, textures or local contrast, as the algorithms (in the computer as well as in the human brain) have to recognize matching features in the individual images. This fails in the case of (semi-) transparent volumes with rather gradual variations of the light intensity, which is mostly the case when working with a microscope and, e.g., biological specimen. The very narrow depth of field of a microscope results in an optical sectioning of thick objects at the focal plane. This can be used to generate a different kind of image set, a so-called focal stack, by gradually shifting the specimen across the plane of focus. Such a stack is a representation of the entire volume, but the individual

slices contain blurred contributions from out-of-focus regions. Removing this blur computationally and thereby reconstructing the original volume is the domain of deconvolution algorithms. They exploit knowledge of the light transport within the optical system, which is in the form of the point spread function or PSF, to reassign the recorded intensities to those slices they were emitted by. This is a slow procedure and involves taking numerous images, which is not possible if the specimen are alive and moving.

If three-dimensional content is to be stored in a single recording of a planar sensor, be it chemical or digital, the depth coordinate has to be coded into the flat image. Examples for such a coding are holograms, where the wavefronts emanating from an object interfere with a reference beam of light. This generates fringe patterns carrying information on the original 3-D volume, which are recorded by a high-resolution medium.

A technique that circumvents using coherent light sources and complex setups and that has recently gained considerable momentum is light field imaging by plenoptic cameras. The light field is a scalar field and describes the transport of light intensity – the radiance – along rays in space, as a function of position and direction. The concept of the light field is old, and so are some of the proposed techniques for recording it: The term was first introduced in 1939 by Gershun [7], and the use of arrays of lenses for light field capturing dates back to the work on integral photography by Lippmann in 1908 [11]. However, the technical skills for precisely tooling small lenses were limited by then, and so was the practical usability of the idea. Massive improvements in manufacturing technology and the boost in computational power in the last decades led to the development of digital light field cameras [1, 14–16].

These cameras use arrays of microlenses close to the sensor to code the lost directional information into the captured raw images. It allows to derive the depth of the scene, and for transparent objects, like the specimen in microscopy, the 3D intensity distribution within the volume can be reconstructed [10]. This is a scanless technique based on a single snapshot recording, with the attractive potential of investigating dynamic processes in three dimensions.

Reconstruction methods rest upon deconvolution algorithms and require the point spread function of the optical system, as outlined briefly for classical microscopy. In more recent approaches of light field deconvolution, the PSF is stored conveniently in a 5D matrix [3]. The iterative updates within the algorithm additionally demand the transpose of this matrix, which is not readily available and needs to be derived in beforehand. This is computationally burdensome, depending on the pixel resolution of the camera and the design of the microlens array.

The framework of light field deconvolution was proposed first by Broxton et al. [3], and Prevedel et al. [17] published a Matlab code based on this work. A number of variations and improvements of this method have been put forward since then, including (but not limited to) resolution improvements by adding phase masks [4], a

© 2016 ACM. This is the author's version of the work. It is posted here for your personal use. Not for redistribution. The definitive Version of Record was published in, <http://dx.doi.org/10.1145/nnnnnnn.nnnnnnn>.

reconstruction in the phase-space domain with reduced artifacts and considerable speed-up [13] and improved reconstruction quality by incorporating depth-dependant filtering in the deconvolution algorithm [19]. While the theory of light field capturing, the design of the optical setups and the proposed reconstruction algorithms are presented in great detail in the literature, the reader is left alone with the structure of the transposed PSF matrix and how to compute it.

The contribution of this paper is two-fold: First, we clarify the significance of this matrix and its relation to the original PSF, and complement this by hints on how to record a light field PSF experimentally in a suitable matrix structure. Second, we present an efficient and fast algorithm for computing the transposed PSF matrix.

2 LIGHT FIELD IMAGING AND VOLUME RECONSTRUCTION

In a standard photographic camera, single pixels of the sensor (or the grains of a chemical film) integrate the incident light over a certain solid angle. As a consequence, the directional information is lost and the captured images are flat. In a plenoptic light field camera, on the other hand, an additional microlens array is inserted close to the image sensor, as sketched in Figure 1. It has the effect of sorting the light rays, depending on their direction, onto different pixels within the micro images that form beneath the individual lenslets. Two points in object space, marked A and B in the figure, generate distinct spot patterns on the image sensor. The lenslet array acts as an optical multiplexer [20], that codes additional angular information into the two-dimensional raw image recorded by the camera. Comparable to an array of micro cameras, the depth coordinate can be computed based on the relative position of recognizable features within the single micro images [1, 16]. Again, this has the prerequisite of sufficient local contrast within the object.

Alternatively, the extra angular information can be exploited by computationally rendering sets of 2D images [9] with varying optical parameters. This allows to change perspective and focus [8] after

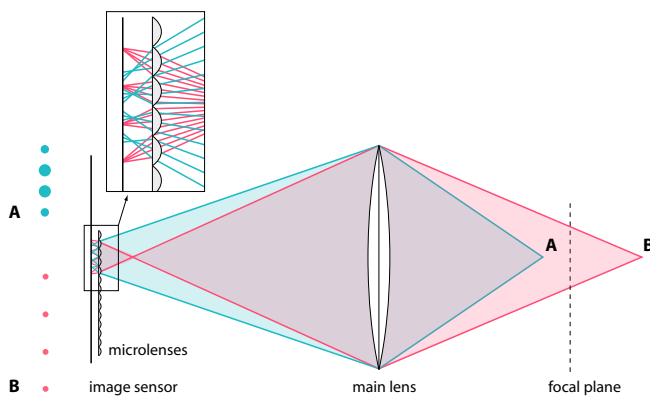


Fig. 1. Sketch of image space, object space and definition of the used dimensions and indices.

the image has been captured, and complete focal stacks can be generated synthetically from a single exposure. This does not require any focus scanning or sequential recording of image series, and is therefore also applicable to dynamic objects. If the focal stacks are used in a deconvolution process, a transparent object space volume may be reconstructed from only one snapshot recording [10].

Clearly, the total information content of a sensor image cannot be simply increased, and consequently a share of the lateral spatial resolution has to be traded in for capturing the depth coordinate. In a plenoptic arrangement, the lateral resolution is proportional to the number of single microlenses in the array, whereas the angular resolution (and consequently, the axial resolution of a reconstructed volume) is proportional to the number of sensor pixels behind each of the lenslets [10].

A technique to mitigate this resolution trade-off was published by Broxton et al. [3], where the method of volume reconstruction from light field data is closely related to a superresolution approach [2], performed in three dimensions. This is termed *light field deconvolution*. It does not require the intermediate step of rendering sets of 2D images, but instead directly operates on the raw images that have been captured by the plenoptic camera.

Interestingly, in the seminal publication by Adelson et al. it is proposed to add a weak diffusor element to the optical system to prevent aliasing due to the low sampling of the light field by the lenslets [1]. This aliasing in fact is, however, the reason and the requirement for the superresolution approach to work [2, 3].

2.1 Image formation and PSF matrix

As outlined briefly, deconvolution in traditional microscopy uses knowledge of the light transport within the optical system to recover the original object volume, which is also done in light field deconvolution. Here the image formation process on the camera sensor is discretized as the linear equation

$$\mathbf{f} = \mathbf{H} \mathbf{g} + \mathbf{b} \quad (1)$$

The 2D image \mathbf{f} , which is formed behind the microlenses, is made up of N_p pixels, that are arranged here in a column vector. It is the result of applying the matrix \mathbf{H} to the 3D intensity distribution within the object volume \mathbf{g} , that is discretized with N_v voxels, again given as a column vector. Additional noise is considered as \mathbf{b} . The sketch in Figure 4 gives an overview of the dimensions and indices in object- and image space that are going to be used throughout this paper. The axial depth coordinate z is aligned with the optical axis, and the lateral directions are labeled x and y .

The light emitted by a single point in space (or a voxel in the discretized world) is transferred through the object space and the optical system and is then recorded as an intensity distribution by the sensor pixels. This distribution is the point spread function (PSF) or the spatial impulse response, which is a function of the 3D position of that point. An example of such a PSF is shown in Fig. 2, where the pixel patterns behind the single lenslets are clearly visible. Both images on the left and right side of the figure were recorded with a light point at the optical axis of the camera, but at different depth positions. The PSFs of all voxels are contained in the matrix \mathbf{H} with dimensions $N_p \times N_v$, which then defines the effect of all voxels in

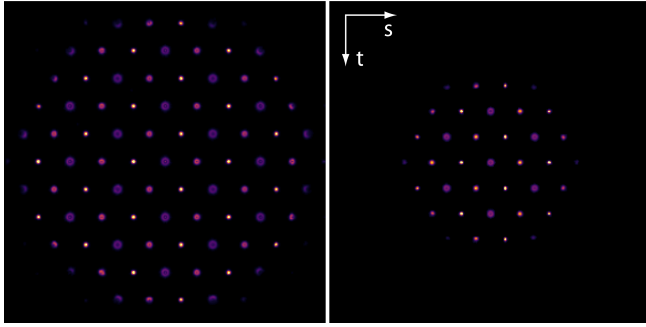


Fig. 2. Examples of intensity distributions produced by a single point in space, so-called point spread functions (PSF), recorded experimentally by a plenoptic camera. The patterns on the left and right side were recorded with a light point at different depth positions along the optical axis. The microlens array consists of three different lens types, which is obvious in the image.

space on all pixels of the sensor.

In practice, the experimental acquisition of \mathbf{H} , performed as a calibration step of a plenoptic camera, requires to capture images of a single light point in space, and subsequently shift the point in steps along all coordinates within the object space [5]. Due to large pixel sizes of the imaging sensor and a high number of voxels in the volume, however, \mathbf{H} would be a huge matrix that is hard to handle. But the required amount of data can be drastically reduced by exploiting the regular arrangement of the microlenses. As a consequence, the pixel patterns produced by single light points are periodically repeating when shifting the point along one of the lateral dimensions, holding the axial dimension constant. This means that for each axial position, \mathbf{H} is defined by a limited number of repeating patterns [3], and the complete volume can be tiled with copies of these patterns. It is therefore sufficient to calibrate the system within a small region that is representative for the used lenslet array. It should be noted that this holds, strictly speaking, only for ideal microscopes, where the objective lens is telecentric and generates orthographic projections. Hence the PSF of the objective alone is shift-invariant and does not depend on the lateral x/y -position [10]. This is not true for photographic systems, where the patterns gradually lose their periodicity towards the edges of the field of view, which may affect the quality of a volume reconstruction.

A further data reduction can be realized during calibration by cropping the recorded raw images to the nonzero pixel values using a rectangular cutout, as shown in Figure 2. This allows to implement the application of the matrix \mathbf{H} , i.e. the projection of a voxel of the volume \mathbf{g} onto the image \mathbf{f} , as a convolution operation. In order to do so, both the light point in space and the cutout region within the raw image have to be shifted likewise during the calibration procedure. From step to step, the cutout region is shifted by a single pixel width, and the point is shifted by an equivalent distance in object space. The latter is defined by the parameters of the optical system in terms of the main lens magnification, which is a function of the focal length and the working distance.

It is interesting to examine the summation of all the elements of \mathbf{H} within one depth plane, which is shown in Figure 3. Here the PSF

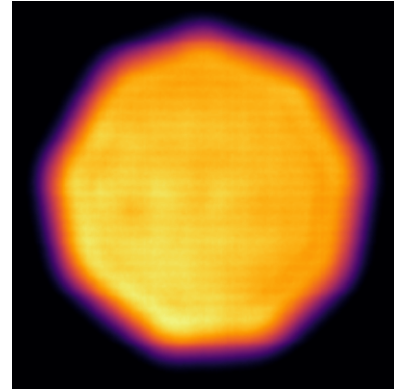


Fig. 3. Summation of all the elements of the PSF matrix \mathbf{H} within one depth plane. The PSF was recorded experimentally using a photographic main lens, and the structure of the aperture constructed from 9 movable blades is clearly seen.

was acquired experimentally with a photographic plenoptic camera (Raytrix R29 with Nikkor 200mm f/4 main lens). By subsequently shifting the point source and the cutout region, the aperture of the main lens is gradually fully lit, so that its design with 9 movable blades is clearly revealed in the image.

2.2 Deconvolution and transposed PSF

Volume reconstruction is an inverse problem that seeks to find the original volume \mathbf{g} from a measured light field \mathbf{f} , using a known PSF matrix \mathbf{H} . This is an ill-posed task, and the inevitable noise prevents a simple inversion of Equation (1). Iterative deconvolution techniques are used instead, with a range of different algorithms, and a summary may be found e.g. in [18]. One example of an algorithm is the classical Richardson-Lucy deconvolution with the following

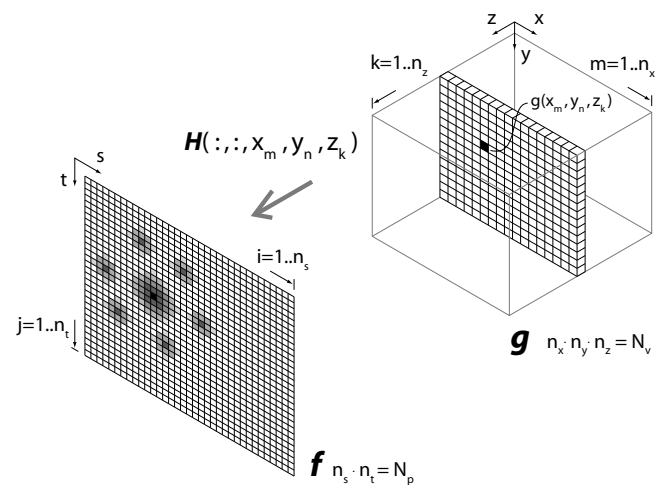


Fig. 4. Sketch of image space, object space and definition of the used dimensions and indices.

update scheme, where k indicates the iteration number [3]:

$$\mathbf{g}^{(k+1)} = \text{diag}(\mathbf{H}^T \mathbf{1})^{-1} \text{diag}(\mathbf{H}^T \text{diag}(\mathbf{H} \mathbf{g}^{(k)} + \mathbf{b})^{-1} \mathbf{f}) \mathbf{g}^{(k)} \quad (2)$$

Commonly, these algorithms involve the transposed PSF matrix \mathbf{H}^T . While \mathbf{H} defines the influence of a single voxel in space on the pixels of the image, \mathbf{H}^T changes the point of view: It takes a single pixel and models the effect of all the voxels on it. In other words, following Helmholtz' reciprocity principle, \mathbf{H}^T reverses the direction of the light rays through the system and formulates a back projection of a pixel through the optical system into the object space.

In the practical implementation of light field deconvolution, the image \mathbf{f} is not defined as a column vector, but as a 2D matrix holding the sensors pixels of the camera. The volume \mathbf{g} is given as a 3D array defining the voxels in the discretized object space. With the notation from Figure 4, \mathbf{H} is conveniently formulated as a 5-dimensional array $H(f_s, f_t, g_x, g_y, g_z)$, where the first two dimensions f_s and f_t contain the pixels in image space, whereas g_x , g_y , and g_z define a position in object space. Transposing this matrix is not done by merely switching rows and columns, but involves interchanging the entries across the first 4 dimensions, independently for each of the z -slices. A number of different procedures for computing \mathbf{H}^T from \mathbf{H} have been proposed as part of published deconvolution codes [13, 17, 19]. However, it is not commented on how the transposing is done, and it is computationally expensive. This is especially significant if the matrices get large, e.g. due to a high pixel count of the sensor, where the calculation of \mathbf{H} may be slower than the actual volume reconstruction (code in [17]). If the camera is calibrated experimentally, several adjustments may be necessary, and a quick calculation of the transpose is required in order to assess the PSF quality.

In the following we present a new algorithm, that takes advantage of the distinct relation between the position of the elements within the original and the transposed matrix. This algorithm is also capable of handling non-symmetric \mathbf{H} matrices, where the dimensions n_x and n_y are not equal, which is the case e.g. for a hexagonal arrangement of the microlenses. We discuss in detail the link between \mathbf{H} and \mathbf{H}^T and benchmark the computational performance of our algorithm.

3 ALGORITHM

In the following, the image plane $f(s, t)$ is discretized with $n_s \cdot n_t = N_p$ pixels and indices $i = 1..n_s$ and $j = 1..n_t$. The object space $g(x, y, z)$ is defined by $n_x \cdot n_y \cdot n_z = N_v$ voxels and corresponding indices $m = 1..n_x$, $n = 1..n_y$, $k = 1..n_z$. Figure 4 illustrates the used dimensions and indices. In this example a voxel $g(x_m, y_n, z_k)$ is mapped by the appropriate z -slice of \mathbf{H} onto the image plane \mathbf{f} . Figure 5 outlines the image formation process in one dimension with a sample matrix \mathbf{H} having a single z -plane, 3 pixels ($n_s = 3$) and 3 positions A, B and C ($n_x = 3$) colored in red, blue and green. The voxels in object space \mathbf{g} (circles) are convolved (full lines) with their respective slices of \mathbf{H} to yield the image \mathbf{f} . Here the dashed boxes represent the sensor pixels, where the contributions (rectangles) from the different voxels are summed up. For each pixel, \mathbf{H}^T defines the influence from the various voxels, which is sketched by the dashed arrows. The same process in two dimensions, again with a single z -plane, is illustrated in Figure 6. Each of the submatrices of

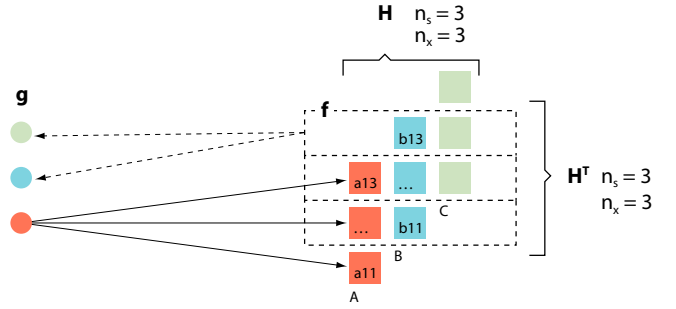


Fig. 5. One dimensional example showing the image formation process: Projection (full arrows) and back projection (dashed arrows) link object- and image space via \mathbf{H} and \mathbf{H}^T .

\mathbf{H} defines how a light point at the respective position in object space is projected onto the image sensor. In this simple case, the number of pixels (n_s, n_t) is equal to the number of spatial positions (n_x, n_y). Without loss of generality, this matrix is now 2D-convolved with a sample object volume \mathbf{g} , here containing all ones, to produce an image \mathbf{f} . In the figure, each rectangular box represents a single pixel of this image that receives contributions from multiple spatial positions. The image is constrained to the 3x3 pixel size of the \mathbf{H} -submatrices, and dashed boxes mark out-of-border pixels. Three of the submatrices of \mathbf{H} are marked with different colors to facilitate the tracking of the matrix elements in the convolution operation. For each pixel we can assemble new submatrices that are built from the contributing elements. This is illustrated in the figure for one of the pixels, marked by a pointer. Such submatrices establish the connection between single sensor pixels and the positions in object space which they are influenced by. By definition, this forms the transposed PSF matrix \mathbf{H}^T . Note that here the physical meaning of the dimensions has changed compared to \mathbf{H} .

In most cases, the image of a single point in object space will have higher numbers of pixels in the f_s - and f_t -dimension than there are slices of \mathbf{H} in the g_x - and g_y -direction. This means $n_s > n_x$ and/or $n_t > n_y$ and has important implications for the transposing procedure. This is illustrated in Figure 7, for the sake of simplicity only in the s - and x -dimension, with a sample matrix \mathbf{H} having $n_s = 5$ and $n_x = 3$. This matrix defines the contributions of 3 points in object space (full circles) being projected (continuous lines) onto each 5 pixels on the camera sensor (full squares) where they sum up to form the image (dashed boxes). The transposed version \mathbf{H}^T reverses this process and represents 3 pixels that are back projected (dashed lines) onto 5 object points. As outlined above, the slices of the PSF \mathbf{H} are periodically repeating due to the regularly arranged microlenses. Under this prerequisite, the additional contributions of the neighboring slices of \mathbf{H} have to be considered (open circles and squares). This means that, e.g., elements of the lowest slice A , colored in red, reappear on the upper end of \mathbf{H}^T .

This effect can be modelled by adding slices around \mathbf{H} in such a way that both in rows and columns the different slices are repeating in a circular fashion. In total, $(n_s - n_x)$ and $(n_t - n_y)$ slices are added in column and row direction, respectively. This is sketched in Figure 8 for a sample matrix \mathbf{H} having $n_s = n_t = 5$ and $n_x = n_y = 3$. The

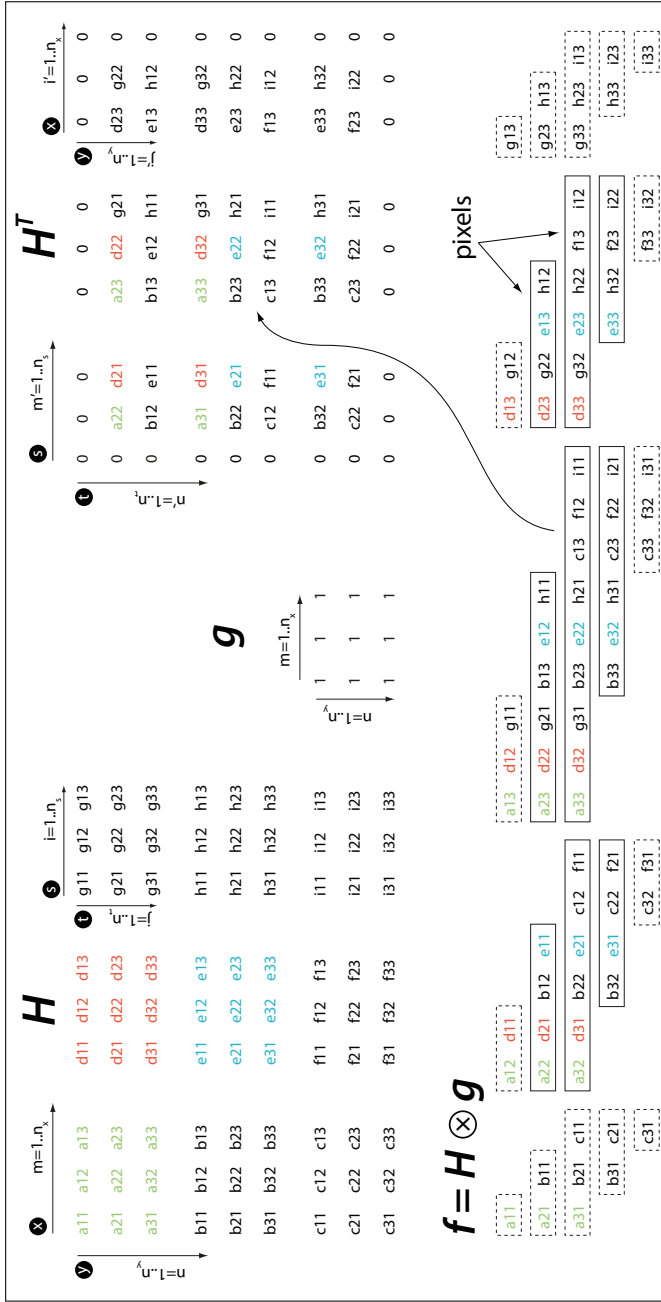


Fig. 6. Illustration of the image formation process, linking the PSF matrix \mathbf{H} , the image \mathbf{f} , and the flipped matrix \mathbf{H}^T via a sample volume \mathbf{g} .

core slices in bold letters within the inner rectangle are completed by additional contributions on the sides.

The algorithm presented in this paper is based on the distinct relation of the positions of the elements within the matrix \mathbf{H} and its transposed counterpart \mathbf{H}^T . For each element of \mathbf{H}^T at position (i', j', m', n') the algorithm finds the corresponding position

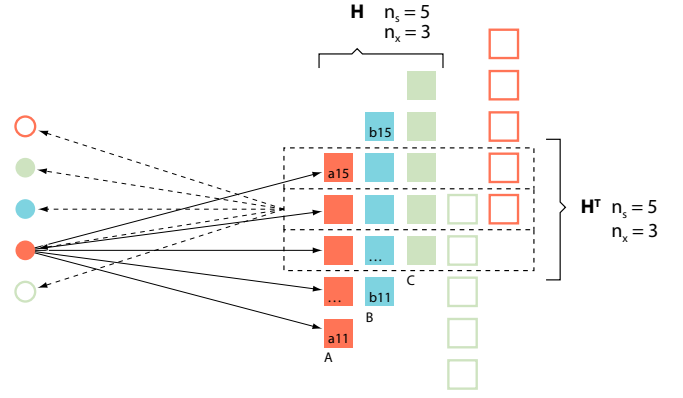


Fig. 7. Interrelation between image- and object space for matrices \mathbf{H} where the pixel size n_s is larger than the number of slices n_x .

(i, j, M, N) within \mathbf{H} , and for each z -plane the new array is constructed by the assignment

$$\mathbf{H}^T(i', j', m', n') = \mathbf{H}(i, j, M, N) \quad (3)$$

With the aid of the auxiliary variables

$$\alpha = m - \left\lfloor \frac{n_s - n_x}{2} \right\rfloor, \quad \beta = n - \left\lfloor \frac{n_t - n_y}{2} \right\rfloor \quad (4)$$

the index M is calculated as

$$M = \begin{cases} \alpha - \left\lfloor \frac{\alpha-1}{n_x} \right\rfloor n_x & \alpha > n_x \\ \alpha + \left\lfloor \frac{1-\alpha}{n_x} \right\rfloor n_x & \alpha \leq 0 \\ \alpha & \text{else} \end{cases} \quad (5)$$

Here $\lceil \cdot \rceil$ and $\lfloor \cdot \rfloor$ denote the *ceiling* and *floor* operation, respectively, and the procedure is looped for $m = 1..n_x + (n_s - n_x)$. This has to be carried out likewise for the index n , resulting in a new value N using n_t, n_y and β . With equation (4), the indices m' and n' are calculated as

$$m' = i - n_x + \alpha + \left\lfloor \frac{n_x - 1}{2} \right\rfloor - \left\lfloor \frac{n_s - n_x}{2} \right\rfloor \quad (6)$$

$$n' = j - n_y + \beta + \left\lfloor \frac{n_y - 1}{2} \right\rfloor - \left\lfloor \frac{n_t - n_y}{2} \right\rfloor \quad (7)$$

within the limits $0 < n' \leq n_y$ and $0 < m' \leq n_x$. The indices i' and j' are found according to

$$i' = n_s - i + (n_s \bmod 2), \quad 0 < i' \quad (8)$$

$$j' = n_t - j + (n_t \bmod 2), \quad 0 < j' \quad (9)$$

These equations have to be looped for $n = 1..n_y + (n_t - n_y)$, for $m = 1..n_x + (n_s - n_x)$, for $i = 1..n_s$ and for $j = 1..n_t$.

Both the new and the previous algorithms require the spatial dimensions n_x and n_y to be odd-numbered.

As can be seen in Figure 6, some elements of \mathbf{H} are dropped in the process and a zero-border of width $(n_x - 1)/2$ and $(n_y - 1)/2$ in column and row direction, respectively, forms around \mathbf{H}^T . This can be prevented by padding each slice of \mathbf{H} symmetrically with $(n_x - 1)$ and $(n_y - 1)$ zeros and taking the central part of the resulting \mathbf{H}^T . The transposing is fully reversible and processing \mathbf{H}^T yields the original matrix \mathbf{H} . The complete transposing procedure in pseudocode

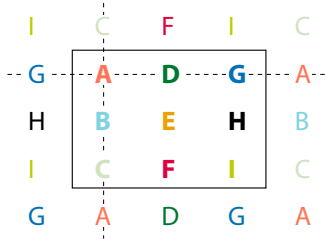


Fig. 8. Case with $n_s > n_x$ or $n_t > n_y$: The input matrix \mathbf{H} (inner rectangle) is extended by additional slices.

is given in Figure 9. A colon indicates a simultaneous operation on all z -planes.

The result of the transposing operation is presented in Figure 10. It shows two slices of the transposed matrix \mathbf{H}^T , computed from the data given exemplarily in Figure 2. These slices define the back projection of single pixels into object space, at identical depth planes, but different lateral (s, t) pixel positions. The off-center slice on the right side of the figure clearly shows line patterns due to diffraction at the main lens aperture.

As a side note, if all slices of \mathbf{H}^T within one depth plane are summed up, the result is identical to the image given in Figure 3, except for

```

procedure CalcHT ( $\mathbf{H}, \mathbf{H}^T$ )
  for  $m = 1 \dots n_x + (n_s - n_x)$  do
     $M \leftarrow$  eq. 5
  end for
  for  $n = 1 \dots n_y + (n_t - n_y)$  do
     $N \leftarrow$  eq. 5     $\triangleright$  with  $n_t, n_y, \beta$ 
  end for
  for  $i = 1 \dots n_s$  do
     $i' \leftarrow$  eq. 8
    for  $m = 1 \dots n_x + (n_s - n_x)$  do
       $m' \leftarrow$  eq. 6
    end for
    for  $j = 1 \dots n_t$  do
       $j' \leftarrow$  eq. 9
      for  $n = 1 \dots n_y + (n_t - n_y)$  do
         $n' \leftarrow$  eq. 7
      end for
      for all  $0 < m' \leq n_x, 0 < n' \leq n_y$  do
        for all  $0 < i', 0 < j'$  do
           $\mathbf{H}^T(i', j', m', n', :) = \mathbf{H}(i, j, M, N, :)$ 
        end for
      end for
    end for
  end for
end procedure

```

Fig. 9. Algorithm in pseudocode.

a rotation by 180° . This is due to reversing the projection direction, which effectively exchanges the entrance and exit pupils of the optical system.

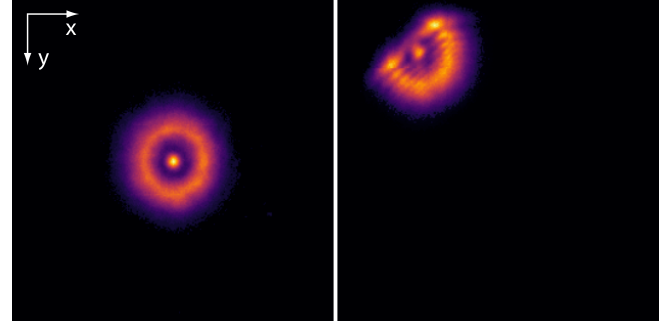


Fig. 10. Slices of the transposed PSF matrix \mathbf{H}^T at different lateral positions, but identical axial depth. The off-center slice on the right side clearly shows diffraction at the main lens aperture.

4 PERFORMANCE

The performance of the new algorithm was tested with sample matrices \mathbf{H} of various sizes, filled with random numbers. In all cases, identical pixel sizes n_s and n_t and, except for the last case, identical volume sizes n_x and n_y were used with n_z set to 11. The transposed matrices \mathbf{H}^T were computed on a desktop PC having an Intel i7-6700K CPU at 4 GHz and 48 GB of memory. The same computations were done using the transposing procedures which are part of the codes published in Refs. [13, 17, 19]. All algorithms were written in MATLAB (version 2019a). In all cases, the results on \mathbf{H}^T calculated by the different routines are identical, and the required computation times, measured in seconds, are given in columns 4, 5, 6 and 7 of Table 1. As the procedure published in [19] takes advantage of the sparseness of actual \mathbf{H} matrices, the computation times for such sample PSFs is given additionally in parentheses.

For all tested matrix sizes, our new algorithm is considerably faster. Especially for high values of n_x and n_y , the algorithms from Refs. [17, 19] are very slow and a significant speedup is achieved by the presented new procedure. Modern commercial plenoptic cameras feature high resolution image sensors with a high number of pixels

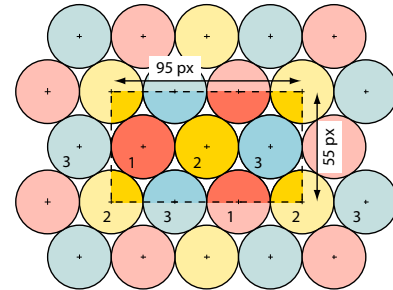


Fig. 11. Sketch of a microlens layout with a hexagonal arrangement and three different types of lenslets, mounted e.g. in a Raytrix R29 camera. The dashed box marks the representative region.

under each microlens. As an example, the R29 by Raytrix has 31x31 pixel micro images in a hexagonal arrangement and features three different types of microlenses. This layout is sketched in Figure 11. The representative region for such a lens pattern is indicated as a dashed rectangle, and requires to consider 95x55 positions in the n_x and n_y dimension. The case in the last row of Table 1 is an example for a PSF matrix \mathbf{H} acquired experimentally with an R29 camera, and with the new algorithm the transposing is done in reasonable 24 seconds. Here n_x and n_y are not equal so that this case cannot be treated by the other algorithms.

Table 1. Computation time in seconds for various sizes of the matrix \mathbf{H} , filled with random values. In all cases the number of z -slices n_z is 11. Numbers in parentheses for Ref. [19] give values for actual matrices \mathbf{H} (not random).

n_s, n_t	n_x	n_y	Ref. [17]	Ref. [13]	Ref. [19]	this work
111	11	11	29.0	1.3	14.5 (10.6)	0.2
221	11	11	60.7	6.2	29.1 (24.5)	1.0
331	11	11	166.3	14.3	61.7 (51.5)	2.9
551	11	11	839.0	48.0	198.4 (194.6)	9.1
771	11	11	1679.3	96.1	658.3 (347.2)	19.6
1101	11	11	4382.0	241.3	1164.9 (466.6)	42.6
127	21	21	467.3	3.5	208.7 (152.2)	1.2
187	31	31	4239.0	15.5	1289.0 (880.4)	5.3
307	51	51	88425.0	363.5	25493 (13522)	74.7
181	55	95	-	-	-	24.4

5 CONCLUSION

In this paper we have discussed the significance of the transposed PSF matrix \mathbf{H}^T , which defines a back projection of an image pixel into object space. In light field deconvolution methods, the PSF \mathbf{H} is commonly given as a 5D matrix, and the transposing is non-trivial. We have shown that the position of the individual elements within \mathbf{H} and \mathbf{H}^T are tied by unique relations, which can be exploited to compute \mathbf{H}^T from \mathbf{H} and vice versa. We have presented an algorithm based on these findings, with favorably short computation times compared to other procedures that have been published as part of deconvolution codes. The presented universal algorithm handles arbitrary matrices, independent from the arrangement of the lenslets within the camera's microlens array.

A quick calculation of \mathbf{H}^T is especially beneficial for the assessment of experimentally acquired PSFs that often require several adjustments. The general trend towards higher pixel resolutions of digital imaging sensors also holds for plenoptic light field cameras, with commercial devices available in the range of over 100 megapixels. The associated very large PSF matrices of such future systems can be efficiently transposed with the algorithm derived in the present work.

ACKNOWLEDGMENTS

This work was funded by the German Research Foundation (DFG) under grant No. Lo1772/4-1. The controversial discussions within the High Enthalpy Flow Diagnostics Group (HEFDiG) are highly

appreciated. Thanks for ideas and support to: Stefan Loehle, Arne Meindl, Fabian Hufgard, David Leiser, Igor Hoerner and Felix Grigat.

REFERENCES

- [1] E. Adelson and J. Wang. 1992. Single Lens Stereo with a Plenoptic Camera. *IEEE Transactions on Pattern Analysis and Machine Intelligence* 14, 2 (Feb. 1992), 99–106. <https://doi.org/10.1109/34.121783>
- [2] T. Bishop and P. Favaro. 2012. The Light Field Camera: Extended Depth of Field, Aliasing, and Superresolution. *IEEE Transactions on Pattern Analysis and Machine Intelligence* 34, 5 (2012), 972–986. <https://doi.org/10.1109/TPAMI.2011.168>
- [3] M. Broxton, L. Grosenick, S. Yang, N. Cohen, A. Andalman, K. Deisseroth, and M. Levoy. 2013. Wave optics theory and 3-D deconvolution for the light field microscope. *Optics Express* 21, 21 (2013), 25418–25439. <https://doi.org/10.1364/OE.21.025418>
- [4] N. Cohen, S. Yang, A. Andalman, M. Broxton, L. Grosenick, K. Deisseroth, M. Horowitz, and M. Levoy. 2014. Enhancing the performance of the light field microscope using wavefront coding. *Optics Express* 22, 20 (2014), 24817–24839. <https://doi.org/10.1364/OE.22.024817>
- [5] M. Eberhart and S. Loehle. 2018. Light-Field Imaging for Plasma Wind Tunnel Application. *Journal of Thermophysics and Heat Transfer* 33, 2 (2018), 1–9. <https://doi.org/10.2514/1.5499>
- [6] M. Eberhart and S. Loehle. 2020. 3-D Analysis of Plasma Flows by Light Field Deconvolution. *Journal of Thermophysics and Heat Transfer* submitted (2020).
- [7] A. Gershun. 1939. The Light Field. *Journal of Mathematics and Physics* 18, 1–4 (1939), 51–151. <https://doi.org/10.1002/sapm193918151> arXiv:<https://onlinelibrary.wiley.com/doi/pdf/10.1002/sapm193918151>
- [8] A. Isaksen, L. McMillan, and S. J. Gortler. 2000. Dynamically reparameterized light fields. In *Proceedings of the 27th Annual Conference on Computer Graphics and Interactive Techniques*. ACM Press/Addison-Wesley Publishing Co., 297f?i306. <https://doi.org/10.1145/344779.344929>
- [9] Marc Levoy and Pat Hanrahan. 1996. Light Field Rendering. In *Proceedings of the 23rd Annual Conference on Computer Graphics and Interactive Techniques (SIGGRAPH 96)*. Association for Computing Machinery, New York, NY, USA, 31fi?42. <https://doi.org/10.1145/237170.237199>
- [10] M. Levoy, R. Ng, A. Adams, M. Footer, and M. Horowitz. 2006. Light Field Microscopy. *ACM Trans. Graph.* 25, 3 (2006), 924–934. <https://doi.org/10.1145/1141911.1141976>
- [11] G. Lippmann. 1908. Épreuves réversibles. Photographies intégrales. *Comptes-Rendus Academie des Sciences* 146 (1908), 446–451.
- [12] G. A. Lloyd and S. J. Sasson. 1978. Electronic still camera. U.S. Patent 4131919A.
- [13] Zhi Lu, Jiamin Wu, Hui Qiao, You Zhou, Tao Yan, Zijing Zhou, Xu Zhang, Jingtao Fan, and Qionghai Dai. 2019. Phase-space deconvolution for light field microscopy. *Optics Express* 27, 13 (2019), 18131–18145. <https://doi.org/10.1364/OE.27.018131>
- [14] A. Lumsdaine and T. Georgiev. 2009. The focused plenoptic camera. In *2009 IEEE International Conference on Computational Photography (ICCP)*. 1–8. <https://doi.org/10.1109/ICCPHOT.2009.5559008>
- [15] R. Ng. 2006. *Digital Light Field Photography*. Ph.D. Dissertation. Stanford University.
- [16] C. Perwaß and L. Wietzke. 2012. Single Lens 3D-Camera with Extended Depth-of-Field. In *Human Vision and Electronic Imaging XVII* (Burlingame, California, USA) (*SPIE Proceedings*), Vol. 8291. <https://doi.org/10.1117/12.909882>
- [17] R. Prevedel, Y. G. Yoon, M. Hoffmann, N. Pak, G. Wetzstein, S. Kato, T. Schrödel, R. Raskar, M. Zimmer, E. S. Boyden, and A. Vaziri. 2014. Simultaneous whole-animal 3D imaging of neuronal activity using light-field microscopy. *Nature Methods* 11 (2014), 727–730. <https://doi.org/10.1038/nmeth.2964>
- [18] D. Sage, L. Donati, F. Soulez, D. Fortun, G. Schmit, A. Seitz, R. Guiet, C. Vonesch, and M. Unser. 2017. DeconvolutionLab2: An open-source software for deconvolution microscopy. *Methods* 115 (2017), 28–41. <https://doi.org/10.1016/j.ymeth.2016.12.015>
- [19] A. Stefanoiu, J. Page, P. Symvoulidis, G. Westmeyer, and T. Lasser. 2019. Artifact-free deconvolution in light field microscopy. *Optics Express* 27, 22 (2019), 31644–31666. <https://doi.org/10.1364/OE.27.031644>
- [20] G. Wetzstein, I. Ihrke, and W. Heidrich. 2013. On Plenoptic Multiplexing and Reconstruction. *Int J Comput Vis* 101, 2 (2013), 384–400. <https://doi.org/10.1007/s11263-012-0585-9>